Stacked charge stripes in the quasi-2D trilayer nickelate $La_4Ni_3O_8$

Junjie Zhang[a,1], Yu-Sheng Chen[b], D. Phelan[a], Hong Zheng[a], M. R. Norman[a], and J. F. Mitchell[a,1]

[a]Materials Science Division, Argonne National Laboratory, Argonne, IL 60439; and [b]ChemMatCARS, The University of Chicago, Argonne, IL 60439

Edited by Zachary Fisk, University of California, Irvine, CA, and approved June 21, 2016 (received for review April 28, 2016)

The quasi-2D nickelate $La_4Ni_3O_8$ (La-438), consisting of trilayer networks of square planar Ni ions, is a member of the so-called T′ family, which is derived from the Ruddlesden–Popper (R-P) parent compound $La_4Ni_3O_{10-x}$ by removing two oxygen atoms and rearranging the rock salt layers to fluorite-type layers. Although previous studies on polycrystalline samples have identified a 105-K phase transition with a pronounced electronic and magnetic response but weak lattice character, no consensus on the origin of this transition has been reached. Here, we show using synchrotron X-ray diffraction on high-pO_2 floating zone-grown single crystals that this transition is associated with a real space ordering of charge into a quasi-2D charge stripe ground state. The charge stripe superlattice propagation vector, q = (2/3, 0, 1), corresponds with that found in the related 1/3-hole doped single-layer R-P nickelate, $La_{5/3}Sr_{1/3}NiO_4$ (LSNO-1/3; $Ni^{2.33+}$), with orientation at 45° to the Ni-O bonds. The charge stripes in La-438 are weakly correlated along c to form a staggered *ABAB* stacking that reduces the Coulomb repulsion among the stripes. Surprisingly, however, we find that the charge stripes within each trilayer of La-438 are stacked in phase from one layer to the next, at odds with any simple Coulomb repulsion argument.

charge stripe | charge order | nickelate | strongly correlated materials | transition metal oxides

Competition between localized and itinerant electron behavior is an organizing construct in our understanding of correlated electron transition metal oxide (TMO) physics (1–4). Some of the most compelling phenomenology in these materials occurs in the mixed valent state for the transition metal, which is set by composition, doping, and anion coordination of the metal. Many mixed valent TMOs adopt insulating "charge ordered" states, in which an inhomogeneous but long-range ordered configuration of the charge density condenses from a uniform metallic state (5). The real space pattern of charge order varies by material (6–9), but a typically observed motif is some variety of charge stripes. Such stripes have been observed in cobaltites (10–12), cuprates (13–15), nickelates (16–19), and manganites (20–22), albeit with highly materials-dependent configurations that hinge on a balance among Coulomb, lattice, and magnetic exchange energies. For instance, charge stripes in layered nickelates typically stagger themselves from layer to layer to reduce the collective electrostatic energy arising from the charge disproportionation (9, 18).

Indeed, the case of nickelates plays a prominent role in charge stripe physics (6–9, 16–19, 23–28), because mixed valent Ni^{2+} (d^8) and Ni^{3+} (d^7) compounds, such as $La_{2-x}Sr_xNiO_4$ (LSNO), are structurally and electronically related to high T_c superconductors and thus, have been targeted as potential alternatives to the cuprates. Instead of superconductivity, however, the ground state of such quasi-2D, octahedrally coordinated nickelates is marked by static charge and spin stripes, with a threefold superlattice (SL) periodicity for compositions near x = 1/3 [$La_{5/3}Sr_{1/3}NiO_4$ (LSNO-1/3)] found to be particularly stable (7). Despite this ubiquitous behavior for octahedrally coordinated nickelates, Anisimov et al. (29) have suggested that Ni^{1+} in a square planar coordination with O ions can form an S = 1/2 antiferromagnetic (AFM) insulator that may be doped with low-spin (S = 0) Ni^{2+} holes to yield a superconductor.

To test such ideas, a series of T′ phases $R_{n+1}Ni_nO_{2n+2}$ (R = La, n = 2; R = La, Pr, and Nd, n = 3) with a square planar Ni-O environment was synthesized and studied in polycrystalline form (30–37). None of these materials superconduct. However, one of the members of the series, $La_4Ni_3O_8$ (La-438), undergoes a still incompletely understood phase transition on cooling through 105 K (Fig. 1) accompanied by a dramatic increase in resistivity and a discontinuity in magnetization (35). Based on a range of theoretical treatments (35, 38–43), the transition has been attributed to a spin density wave (SDW) (35) or a low spin- to high spin-driven (LS-HS) metal to insulator transition (37, 38, 41, 44), possibly accompanied by charge disproportionation into two Ni^{1+} sheets sandwiching an Ni^{2+} sheet in the trilayer (Fig. 2*A*) (42). Difficulties remain with each of these potential explanations, and although NMR measurements (36) reveal strongly 2D AFM spin fluctuations developing eventually into long-range order, the nature of the low-temperature magnetic state remains open; neutron powder diffraction shows no magnetic peaks (35). Other fundamental issues connected to nickelate physics are also relevant to La-438, including homogeneity of the hole concentration in the symmetry-inequivalent layers (i.e., layered charge segregation that must be present to some extent because of the different environments of the outer and inner layers); the appropriateness of a mixed valent Ni^{1+}/Ni^{2+} description; the role of ligand holes vis-à-vis more highly oxidized Ni^{3+}-containing oxides, such as LSNO and $LaNiO_3$; $3z^2 - r^2/x^2 - y^2$ orbital polarization; and ultimately, the potential for unconventional superconductivity (45). [Lee and Pickett (45) argue that the weaker d-p hybridization in nickelates renders any such Cu^{2+}-Ni^{1+} analogy

Significance

Competition between localized and itinerant electrons in highly correlated materials can lead to myriad insulating ground states, including spatially inhomogeneous but ordered charge superlattices. In layered transition metal oxides, such charge order can take the form of stripes, which typically arrange themselves in staggered formations to reduce Coulomb repulsion. Having achieved single-crystal growth of the layered nickelate $La_4Ni_3O_8$, we show that its heretofore incompletely understood phase transition is associated with charge stripe ordering. We find that the stripes are stacked directly on top of one another within nickel oxide trilayers but staggered between successive trilayers. A unique, paradoxical ground state results, in which the electrostatic building principle is respected at long range but violated at short range.

Author contributions: J.Z. and J.F.M. designed research; J.Z., Y.-S.C., D.P., and H.Z. performed research; J.Z., Y.-S.C., D.P., H.Z., M.R.N., and J.F.M. analyzed data; and J.Z and J.F.M. wrote the paper with contributions from all authors.

The authors declare no conflict of interest.

This article is a PNAS Direct Submission.

Data deposition: The structural data of $La_4Ni_3O_8$ have been deposited in the Inorganic Crystal Structure Database (Crystal Structure Depot no. 429798). Further details of the crystal structure investigation may be obtained from Fachinformationszentrum Karlsruhe, https://www.fiz-karlsruhe.de/en/leistungen/kristallographie/kristallstrukturdepot.html.

[1]To whom correspondence may be addressed. Email: junjie@anl.gov or mitchell@anl.gov.

This article contains supporting information online at www.pnas.org/lookup/suppl/doi:10.1073/pnas.1606637113/-/DCSupplemental.

moot.] Unfortunately, a lack of single crystals to date has challenged definitive experimental tests and impeded progress on all of these issues.

Here, we present a fresh view of La-438 physics made possible by our newly found ability to grow single crystals of this compound. In particular, using single-crystal synchrotron X-ray diffraction, we find evidence of an SL below the 105-K transition and argue that it is associated with real space ordering of charge. Our results reveal a close connection between La-438 ($Ni^{1.33+}$) and LSNO-1/3 ($Ni^{2.33+}$), including a shared propagation wave vector $\boldsymbol{q}$ = (2/3, 0, 1), ordering of the stripes at 45° to the Ni-O bonds, and a weak coupling along the c axis in a staggered configuration that minimizes Coulomb repulsion between adjacent trilayer blocks separated by ∼6.5 Å. Remarkably, however, our data show that, within the trilayer itself, the charge stripes are stacked in phase with one another, violating the Coulomb repulsion argument at this much shorter (∼3.25 Å) length scale.

Results and Discussion

La-438 single crystals (∼1–2 mm^2 × ∼0.5 mm) were obtained by reducing (4 mol % H_2/Ar gas; 350 °C; 5 d) specimens cleaved from a boule of $La_4Ni_3O_{10}$ that was grown at pO_2 = 20 bar in an optical image floating zone furnace (HKZ-1; SciDre GmbH). The crystals are fragile, likely because of strains and microcracks that develop during the reduction process. Indeed, the structure undergoes a large, highly anisotropic expansion: $\Delta a \sim \Delta b \sim +3.0\%$ and $\Delta c \sim -6.6\%$ (34, 46). Nonetheless, La-438 specimens measured at 15-ID-B of the Advanced Photon Source (APS) definitively showed that they are well-defined single crystals, from which the structure of La-438 was determined (*SI Text*, *Single-Crystal X-Ray Diffraction* and Tables S1 and S2).

At room temperature, La-438 crystallizes in the tetragonal $I4/mmm$ (no. 139) space group with unit cell parameters a_I = 3.9700(5) Å, c_I = 26.092(3) Å, and Z = 2 in agreement with the structure reported by Poltavets et al. (34) from Rietveld refinement on powder neutron data. For consistency with the body of literature on LSNO (18, 47), we henceforth adopt the $F4/mmm$ ($\sqrt{2}\,a_I \times \sqrt{2}\,a_I \times c_I$) description of this high T phase, with the principal axes rotated 45° from the Ni-O bonds (Fig. 2*A*). All Ni atoms are in square planar coordination with Ni-O bond lengths 1.9850(2) Å for Ni(1)-O and 1.9852(3) Å for Ni(2)-O, which are slightly longer than those reported for the $n = 2$ $La_3Ni_2O_6$ (30) and $n = \infty$ $LaNiO_2$ (48) phases. Nominally, the average $Ni^{1.33+}$ oxidation state can be apportioned as Ni^{+} and Ni^{2+} in the outer and inner layers, respectively. However, first principles theoretical considerations argue against this picture (41) along with our experimental data presented below.

Based on single-crystal diffraction measurements, we argue that charge stripe ordering is the underlying mechanism of the semiconductor to insulator transition in La-438. We also find similar signatures in transport, magnetic, and thermodynamic data measured on La-438 crystals as those reported in the unambiguously identified charge stripe phase LSNO-1/3 (7, 16, 27, 49). Fig. 1 shows the temperature dependence of the transport and magnetic properties of as-prepared La-438 single crystals, which are similar to those reported in the works by Poltavets et al. (35) and Cheng et al. (37). [Poltavets et al. (34) pointed out that the La-438 structure does not allow oxygen vacancies, despite its preparation by oxygen deintercalation. The transport, magnetic, and thermodynamic data collected on our La-438 single crystals are in excellent agreement with those reported by Poltavets et al. (35) and Cheng et al. (37), confirming that our samples are oxygen stoichiometric.] The in-plane resistivity (Fig. 1*A*) reveals a semiconducting behavior above a transition at 105 K and a highly insulating behavior below this transition. The abrupt localization of charge below the transition is qualitatively similar to that observed in LSNO-1/3 (16) with the onset of charge stripes. We note that Cheng et al. (37) suggest that poor grain connectivity in their cold-pressed polycrystalline La-438 samples leads to an anomalously high resistance for T > 105 K and argue from thermopower measurements that the true state in this high T regime is metallic.

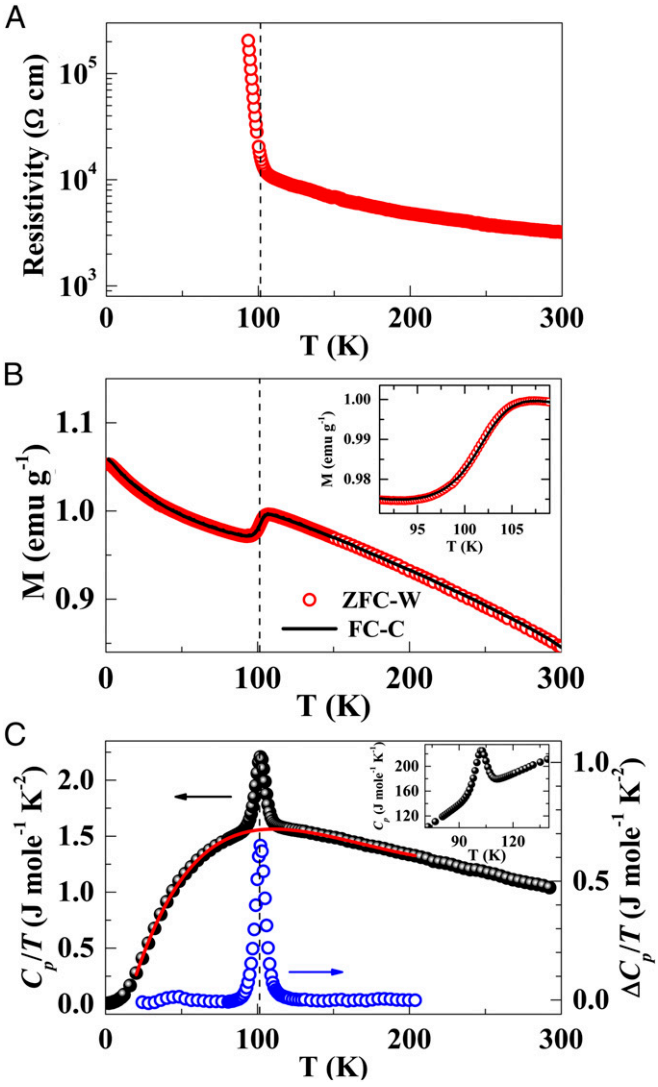

Fig. 1. Temperature dependence of selected physical properties of La-438. (*A*) Electrical resistivity in the *ab* plane. (*B*) In-plane magnetic susceptibility for 5 T. *B*, *Inset* shows the details around the transition. FC-C, data collected on cooling under field (black curve); ZFC-W, data collected on warming after zero field cooling (red circles). (*C*) Heat capacity C_p/T vs. T in zero field. *C*, *Inset* shows the λ-like shape of the 105-K anomaly in C_p. Open blue circles, difference between the data and the fit; red curve, polynomial background fit; solid back points, data.

Our data show a similar high resistance, which could result from poor connectivity across a strain-induced network of microcracks created during the reduction process. Nonetheless, the temperature dependence is not that of a metal. The semiconducting behavior above the charge stripe ordering transition may signify the presence of short-range correlations among localized electrons, and such behavior is also observed in LSNO-1/3 (27). For instance, Abeykoon et al. (23) have reported that dynamic charge stripe correlations in LSNO-1/3 can survive up to $\sim 2T_{CO}$ (∼480 K). The magnetic susceptibility (Fig. 1*B*) shows a step at 105 K, which is again qualitatively similar to that observed in LSNO-1/3 (49). Although LSNO-1/3 shows a slope change in $d\chi/dT$ at $T_{SO} \sim 194$ K < $T_{CO} \sim 239$ K (49), we find no evidence for such in La-438 below 105 K. It is possible that La-438 does not have such a spin ordering transition or that it is coincident with the localization transition at 105 K. A Curie–Weiss analysis of the high-temperature data can be found in *SI Text*, *Magnetization* and Figs. S1 and S2.

The heat capacity of an La-438 single crystal is presented in Fig. 1*C*; the phase transition at T_{CO} is clearly indicated by a prominent anomaly. C_p/T is independent of the magnetic field up to 9 T within the experimental resolution (*SI Text*, *Heat Capacity* and Fig. S3), a behavior similar to that reported for LSNO-1/3 (49). The λ-like shape of the anomaly in C_p (Fig. 1*C*, *Inset*) and the absence of thermal hysteresis in the magnetic susceptibility (Fig. 1*B*, *Inset*) evidence a second-order phase transition, as was reported for charge stripe formation in LSNO-1/3 (49). To estimate the entropy change of the transition, we have phenomenologically fit the behavior above and below with a fifth-order polynomial and subtracted this background (*SI Text*, *Heat Capacity*). Integrating the area under the resultant peak yields ΔS = 5.93 J mol^{-1} K^{-1} (1.98 J mol^{-1} K^{-1} Ni^{-1}), which agrees well with that found by Poltavets et al. (35) (5.96 J mol^{-1} K^{-1}). The entropy change per Ni in La-438 is identical to that found by Klingeler et al. (49) in LSNO-1/3 (2.0 ± 0.3 J mol^{-1} K^{-1} Ni^{-1}), which has been attributed to the condensation of the short-range, fluctuating charge stripes that exist above T_{CO}. Alternative explanations that ignore the potential influence of short-range order, such as a 3D Néel transition (ΔS = 3.84 J mol^{-1} K^{-1} Ni^{-1}), an SDW transition ($\Delta S \sim T_{CO}/T_F \sim 0.08$ J mol^{-1} K^{-1}) (50, 51), or an LS-HS transition (ΔS = 1.63 J mol^{-1} K^{-1} Ni^{-1}), are not supported by the data (*SI Text*, *Heat Capacity*). The agreement of the entropy changes through the transition in La-438 and stripe ordered LSNO-1/3 is hardly a coincidence, and we will show below compelling evidence for charge stripe formation in La-438.

Fig. 2 *B–D* shows the temperature dependence of the unit cell parameters in the range 82–120 K extracted from Rietveld refinement of high-resolution X-ray powder diffraction data (*SI Text*, *High-Resolution Powder X-Ray Diffraction* and Fig. S4). No symmetry change was observed in the powder data below the transition in this temperature range. However, a clear increase of the *a*-axis length (~0.029%) and unit cell volume (~0.02%) and a decrease of the *c*-axis length (~0.038%) are observed when cooling through the 105-K transition, with a concomitant drop in *c*/*a* (~0.068%). Our data are consistent with those published by Cheng et al. (37) and reflect a weak lattice contribution to the transition. Fig. 2 *E–G* shows the La-O and Ni-O bond lengths as a function of temperature. Pronounced but smooth changes in the bond lengths of La1-O1 (~0.003 Å), Ni1-O1 (<0.001 Å), and Ni2-O2 (<0.001 Å) are observed, but no changes outside the noise are observed in La1-O2, La2-O2, and La2-O3. This behavior shows that the structural changes that occur through the transition are isolated to the Ni-O trilayer blocks, with the rock salt LaO layers acting as weak structural links between these blocks. We note that the sign of the change in unit cell parameters and Ni-O bond distance on cooling is consistent with the spin-state transition model proposed by Lokshin and Egami (44) and developed theoretically by Pardo and Pickett (41), in which $x^2 - y^2$ orbitals become more electron-rich. If such a picture is correct, however, the charge redistribution is associated with a remarkably small magnitude of the lattice response.

With an average oxidation state of 1.33+, square planar-coordinated La-438 is separated by an integral charge from the average oxidation state of 2.33+ in octahedrally coordinated LSNO-1/3, which develops a charge and spin stripe-ordered ground state. It is, thus, intriguing to consider that analogous ordering of charges and spins could be occurring in this square planar coordinated trilayer system electronically controlled by a 1/3-hole doping beyond a uniform Ni^{1+} background. We now provide synchrotron X-ray diffraction evidence that supports such a picture and argue that real space ordering of charge is the cause of the semiconductor to insulator transition in La-438.

Fig. 3*A* shows an *hk*0 plane measured at 95 K. In addition to the fundamentals at (2, −4, 0), (4, −4, 0), (2, −6, 0), etc., sharp SL reflections are observed between these fundamentals spaced evenly at an interval of $a^*/3$. Refinement of the positions against ~400 SL reflections ($I \geq 3\sigma$) gives q = 0.333(1). SL spots are observed along both $\boldsymbol{a}^*$ and $\boldsymbol{b}^*$, reflecting the mixture of two 90°-oriented orthorhombic domains expected on lowering of symmetry from tetragonal to orthorhombic. The presence of such distinct stripe domains rotated by 90° with respect to one another has also been observed in the single-layer Ruddlesden–Popper

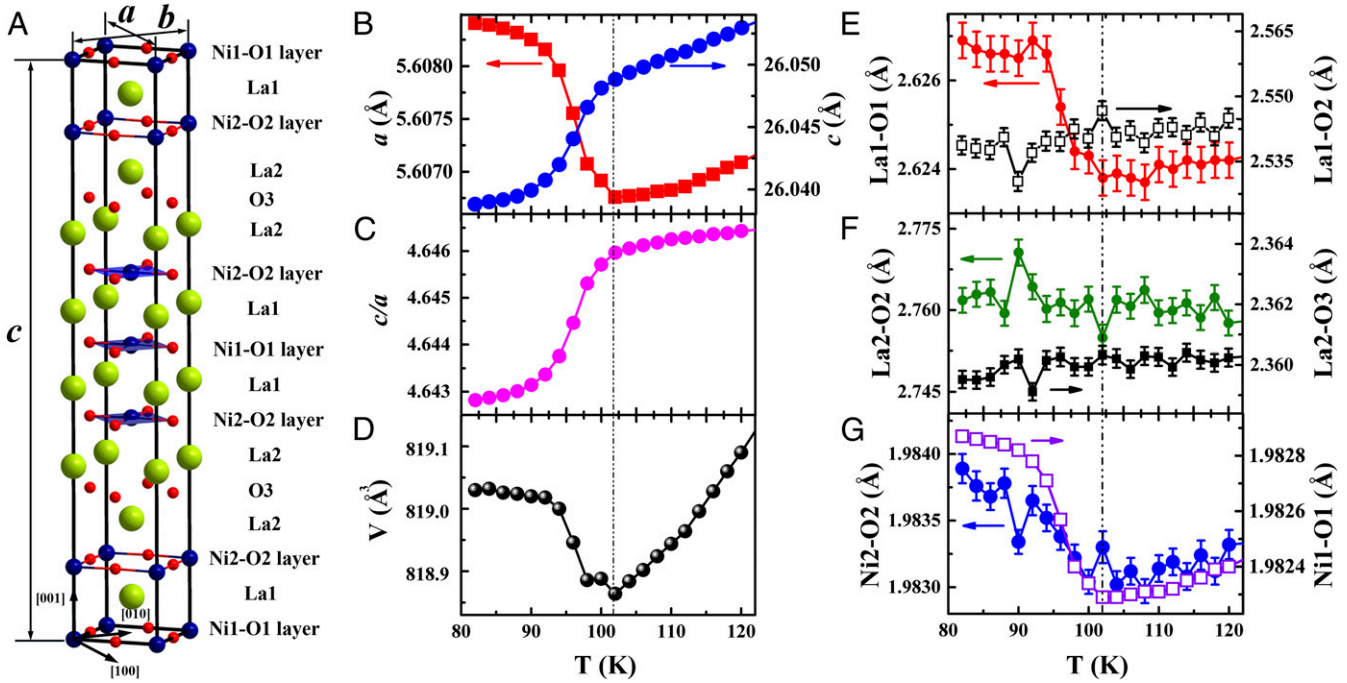

Fig. 2. Crystal structure of La-438. (*A*) The *I*4/*mmm* unit cell is highlighted with solid lines, and the *F*4/*mmm* setting used in this work is identified by the lattice vectors *a*, *b*, and *c*. Temperature dependence of the (*B–D*) unit cell parameters and (*E–G*) bond distances extracted from Rietveld refinement on high-resolution synchrotron X-ray powder diffraction data. Error bars represent the estimated SD from the refinement, and they are smaller than symbols for the unit cell parameters (*a*, *c*, and *V*).

(R-P) phases (47). The resulting pattern in the *hk*0 layer, thus, appears as squares of SL peaks along the zone edge, corresponding to the [100] direction in real space, or 45° to the Ni-O bonds. A line cut along (h, −3, 0) (Fig. 3*I*) shows that these SL reflections are absent above the 105-K transition. In contrast to the sharp reflections seen in the *hk*0 projection, the SL peaks become broadened along $\boldsymbol{c}^*$ as shown in the (h + 8/3, h − 8/3, l) plane (Fig. 3*C*). Because the widths of the main peaks and SL peaks are similar in the *ab* plane, one cannot differentiate a finite correlation length from long-range order. Along $\boldsymbol{c}^*$, however, the SL peaks are significantly broader than the main Bragg peaks. Analysis of the peak width (*SI Text*, *Correlation Length* and Fig. S6) yields a finite correlation length of ∼8 Å along the *c* direction, which is the same order as the distance between neighboring trilayer blocks. Thus, the qualitative appearance is consistent with the expected $\xi_{ab} >> \xi_c$, which was likewise found in LSNO-1/3 (19). We might expect that short-range fluctuating stripes will form above 105 K before condensing, again like LSNO-1/3 (23). The close agreement of the entropy changes through the transition to long-range order between La-438 and LSNO-1/3 corroborates this supposition.

The distribution of positions and intensities of the SL reflections provides a means to assess the real space arrangement of the stripes (i.e., the intra- and interlayer charge stacking). Consider first the stacking of charges within the trilayer, a unique feature of La-438 vis-à-vis LSNO-1/3. Although Coulomb repulsion arguments favor a staggering of the charge from layer to layer, our diffraction data conclusively show that the charges are stacked in phase within the trilayer. Fig. 3 *B* and *D* shows simulations of the scattering from a stacked charge trilayer model assuming $\boldsymbol{q}$ = (2/3, 0, 1). This propagation vector produces a threefold diagonal stripe pattern in the *ab* plane oriented at 45° to the Ni-O bonds, which is in agreement with the observations. Intensity variation along $\boldsymbol{c}^*$ takes maximum values at positions

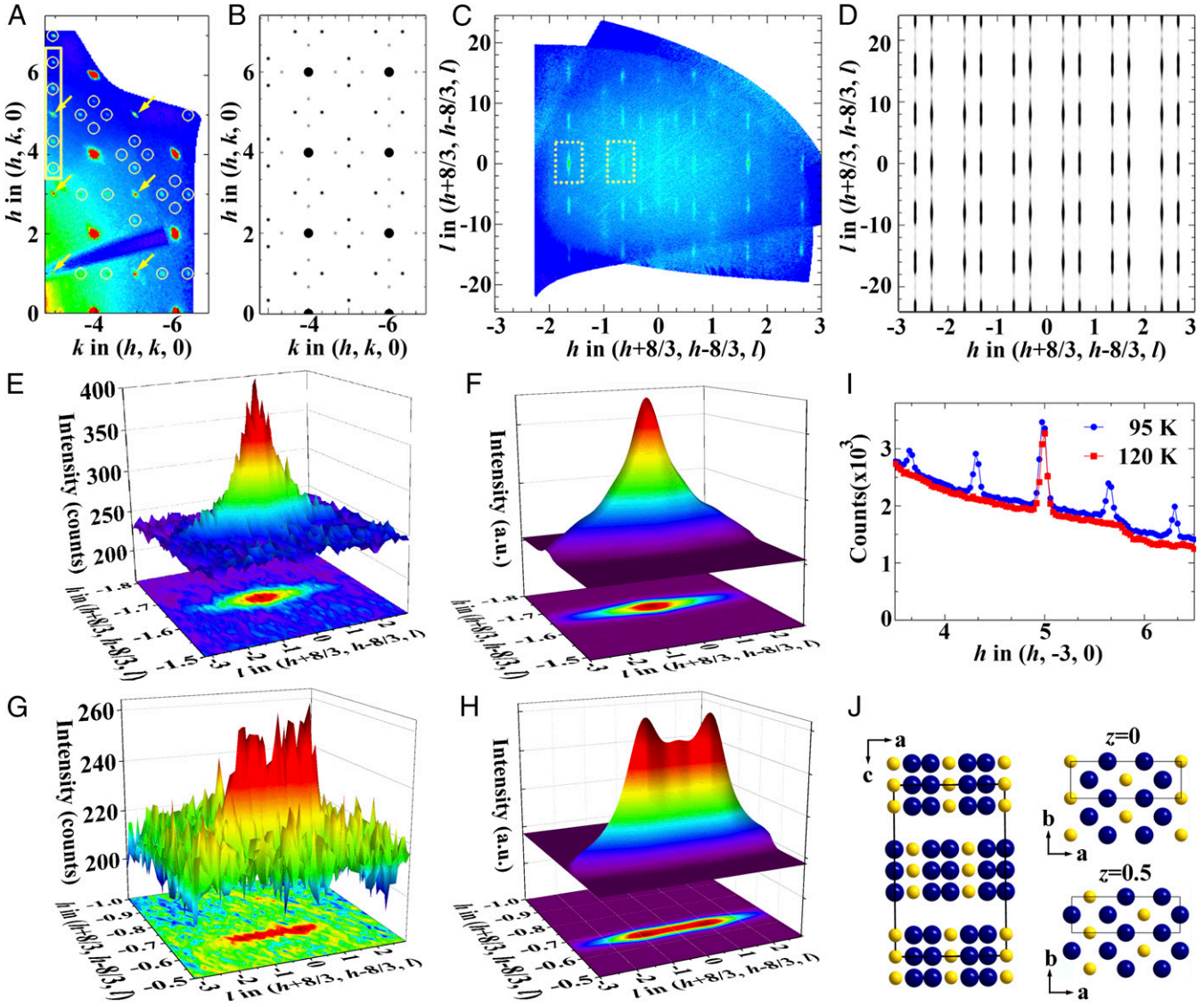

Fig. 3. Charge stripe ordering in La-438. (*A* and *C*) Reconstructed (*hk*0) and (h + 8/3, h − 8/3, l) planes (*F*4/*mmm* notation) measured below 105 K at 15-ID-B. Note that intensity at the forbidden peaks [e.g., (1, −5, 0), (3, −5, 0), (5, −3, 0), . . .], as indicated by yellow arrows in *A*, results from leakage of intensity from allowed Bragg reflections at positions (h, k, ±1) (*SI Text*, *Diffuse Scattering Along c**and Fig. S5). (*E* and *G*) Measured SL peaks at (1, −4.333, 0) and (2, −3.333, 0) as indicated by dashed yellow rectangles in *C*. (*B*, *D*, *F*, and *H*) Simulated diffraction patterns based on the charge stripe model shown in *J*. The size of the spots in *B* indicates the intensity. (*I*) Intensity along the line (h, −3, 0) at 95 K (blue circles) and 120 K (red squares). (*J*) Charge stripe model in real space. Yellow spheres represent areas of higher valence than the average 1.33+, and blue spheres represent areas of lower valence than the average 1.33+. Solid rectangles denote the charge stripe supercell.

spaced by $\Delta l = 8$, a consequence of the $c/8$ spacing of the layers within a trilayer. Importantly, the maxima along $\boldsymbol{c}^*$ appear at $l = 8n$, in agreement with the data presented in Fig. 3*C*. In contrast, a model in which the charges are staggered within the trilayer yields intensity maxima at $l = 4 + 8n$ (*SI Text*, *Charge Stripe Stacking Models* and Fig. S7), inconsistent with the experimental data. Other stacking models were tested (*SI Text*, *Charge Stripe Stacking Models* and Figs. S8 and S9) but likewise, failed to match the observed scattering. Stacking of charge is counterintuitive within a framework of a simple electrostatic model. Indeed, charge stacking in manganites adopting the zig-zag CE charge, orbital, and magnetic ordered state was explained by invoking an intersite Coulomb repulsion of lesser importance than the kinetic energy (double exchange) and magnetic interactions along the Mn^{3+}/Mn^{4+} stripes (21). In the case of the La-438 nickelate, a similar mechanism might apply. A free energy gain is possible from the d^8 sites if they stack on top of one another, because their partially occupied $3z^2 - r^2$ orbitals would generate a net bonding interaction along $\boldsymbol{c}$. A related bonding picture was suggested by Pardo and Pickett (38), although their particular model should not exhibit the charge modulation found here.

We turn now to the intertrilayer stacking of charges, which in single-layer LSNO-1/3, follows a body-centering pattern schematically shown in figure 3 in ref. 9 and figure 10C in ref. 18. This arrangement minimizes the Coulomb repulsion among the stripes. Our data indicate that La-438 adopts a competing *ABAB* stacking (*A* and *B* represent a trilayer) shown schematically in Fig. 3*J*. Fig. 3*A* shows that the SL spots in the *hk*0 plane have a nonuniform intensity distribution with reflections ($h \pm 1/3, k \pm 1$, 0) (and equivalents for the 90° rotated domain), where (h, k, 0) is an allowed reflection of *F*4/*mmm*, appearing more intense than those with index ($h \pm 2/3, k$, 0). This distribution of intensity can be reproduced (Fig. 3*B*) by a model with *ABAB* stacking of the stripes along $\boldsymbol{c}$, akin to that shown in figure 10B in ref. 18. Note that this *ABAB* stacking sequence permits even l reflections and thus, differs from the LSNO-1/3 stacking pattern in which bond- and site-centered stripes alternate along $\boldsymbol{c}$, for which odd l reflections only are observed.

Additional support for the *ABAB* model can be found by interrogating the l dependence of the peak intensities. Fig. 3 *E* and *G* shows intensity plots along $\boldsymbol{c}^*$ in the vicinity of the (1, −4.333, 0) and (2, −3.333, 0) SL reflections, respectively. Although both are broad, there is a clear qualitative difference in the appearance of these peaks: the former consists of a single maximum, whereas the latter appears as a poorly resolved doublet. The simulated patterns for these reflections are shown in Fig. 3 *F* and *H* and in good agreement with the corresponding data. Inspection of the simulated data in the absence of broadening shows that each peak is actually a triplet with intensity centered at $l = -1, 0, 1$. In the case of (1, −4.333, 0) and its equivalent SL reflections, the maximum intensity is located at $l = 0$, whereas for (2, −3.333, 0), the maximum intensity is located at $l = -1$ and 1. Hücker et al. (18) have pointed out that the difference between a double-period *ABAB* and a triple-period *ABCABC* stacking is set by the second neighbor interaction, which is expected to be weak. Because of the short correlation length of the charge stripes along *c*, it is almost certain that La-438 contains alternative stacking sequence faults (e.g., *ABC* and *AA*); the observed SL pattern in the (*hk*0) plane, however, guarantees that *ABAB* dominates. Although La-438 adopts a different stacking than that found in LSNO-1/3, the stacking of charge from trilayer to trilayer in the observed pattern likewise minimizes the Coulomb repulsion.

We have established that a real space ordering of charge is the underlying mechanism of the semiconductor to insulator transition in La-438. We also note that the related single-layer R-P nickelates as well as the cuprates typically exhibit spin stripes in addition to the charge stripes. Thus, it is reasonable to speculate that La-438 would likewise show similar behavior. In LSNO-1/3, the spins order at a lower temperature than the charge, which was evidenced by a signature in the magnetic susceptibility. The absence of such a signature in La-438 suggests that spin stripes, if they exist, order at the same temperature as the charge stripes. Testing for spin stripe ordering will require spin-polarized neutron measurements, because the in-plane wave vectors of the two orders are coincident for this three period case (6).

Conclusion

Our observations offer a fresh perspective on the ground state and origin of the phase transition in La-438. Primarily, we find that the low-temperature ground state of La-438 is a charge stripe ordered insulator, akin to those found in LSNO-1/3, and that this real space order into charge stripes is the cause of the semiconductor to insulator transition at 105 K. We find that this inhomogeneous charge distribution takes the form of stacked charge stripes within the trilayer, which then stagger between trilayers along $\boldsymbol{c}$ in an *ABAB* sequence. Thus, when framed solely within the context of a simple inverse-square law, La-438 adopts a paradoxical ground state, in which the Coulomb interaction is minimized at long distances but not at short range. Although a full quantitative understanding of this stripe organization will require theoretical input, one possibility is that bonding among partially occupied $3z^2 - r^2$ orbitals within the trilayer, which favors locking the charge into this stacked pattern, outweighs the short-range electrostatic energy.

Additional confirmation of the connection between La-438 and LSNO nickelate physics will require understanding of the magnetic ground state of La-438, which should likewise exhibit the same in-plane wave vector; neutron and magnetic X-ray scattering measurements are planned to test this possibility. Finally, our single crystals provide a platform to address a broader set of questions about La-438, including orbital polarization and related questions regarding spin-state and ligand hole contribution. It may also be possible to dope electrons into these crystals to explore the impact on the charge ordered ground state.

Materials and Methods

Physical Properties. Magnetic susceptibility measurements were performed on single crystals using a Quantum Design MPMS3 SQUID Magnetometer. Zero-field cooled and field cooled data in the *ab* plane and out of plane were collected between 1.8 and 300 K under an external field of 0.01, 0.1, 1.0, and 5.0 T. High-temperature (300–795 K) magnetic susceptibility data were collected on MPMS3 equipped with an oven under a magnetic field of 1.0 T. The electrical resistivity was measured in the *ab* plane of the La-438 single crystals under zero applied magnetic field using the standard four-probe alternating current (AC) technique on a Quantum Design Physical Properties Measurement System (PPMS). The heat capacity measurements were carried out in the PPMS using the relaxation method under magnetic fields of 0 and 9 T.

X-Ray Diffraction Experiments. Single-crystal X-ray diffraction data were collected with an APEX2 Area Detector using synchrotron radiation (λ = 0.41328 Å) at beamline 15-ID-B at the APS, Argonne National Laboratory. A single crystal with dimensions of ∼5 μm on an edge was used to determine the structure at room temperature. To observe the SL peaks below the 105-K transition clearly, larger single crystals (∼20 μm on edge) and longer exposure times (e.g., 2.0 s/0.2°) were used. In this case, many Bragg peaks were found to overflow because of the limited dynamic range of the CCD detector (maximum 65,536) and the extreme intensity ratio of the Bragg/SL peaks (∼10^5). Several single crystals were used in this experiment, and the SL peaks are reproducible. Data were collected at room temperature first, and then, the samples were measured in the range of 90–200 K by flowing nitrogen gas and the range of 15–70 K by flowing helium gas; Φ scans were used, and 1,800 frames were collected for *q*-vector refinements.

Variable Temperature High-Resolution Powder X-Ray Diffraction. High-resolution powder X-ray diffraction data were collected on pulverized La-438 crystals at beamline 11-BM (APS) in the range of $0.5° \leq 2\theta \leq 36°$, with a step size of 0.001° and step time of 0.2 s (*SI Text*, *High-Resolution Powder X-Ray Diffraction*).

Charge Stripe Ordering Simulations. The structure factors for SL reflections were calculated by construction of SL unit cells with a modulation of charge imposed on the nickel sites, such that a charge disproportionation results in the *ab* plane. The stacking of stripes along the *c* axis is usually controlled by minimization of the Coulomb repulsion between the charge stripes (52, 53), leading to staggering, although other factors could lead to an alignment instead (21). Therefore, in the case of La-438, we tested the four most

reasonable models: stacked/staggered stripes within a trilayer and stacked/staggered stripes between the trilayers (*SI Text*, *Charge Stripe Stacking Models*). Within each plane, we heuristically assign a valence of +1 or +2 for the nickel sites; thus, charge stripes run parallel to the *b* axis and perpendicular to the *a* axis with a . . . +1/+1/+2/+1/+1/+2 . . . pattern. Although only an approximation of the true charge state of the stripes, this approach allows for a qualitative comparison with the observed pattern of SL reflections and thus, provides insight into which models are consistent with experimental data and which can be eliminated. It is worth noting that the actual charge difference is almost certainly not one but rather, much smaller. This approximation only influences the scale factor linking the intensities of the main Bragg peaks and the SL peaks; it does not change the relative intensity distribution of the pattern, including the position of the maxima. We have applied a Lorentzian broadening along c^* using the finite correlation length discussed in *SI Text*, *Correlation Length*. The following simplifications have been used: we have not included any lattice response, a real scattering length has been considered for each atom, no effort has been made to correct for the energy- or momentum-dependent scattering length, and Debye–Waller factors were not incorporated.

ACKNOWLEDGMENTS. We thank Mr. Wenyang Gao for his help with the synchrotron X-ray single-crystal measurements at 15-ID-B; Dr. Mati Meron for his help on instrument resolution determination; Dr. Saul Lapidus for his help with the high-resolution X-ray powder diffraction at 11-BM; and Drs. V. Pardo, W. E. Pickett, J. W. Freeland, S. Rosenkranz, A. S. Botana, Y. Ren, and C. D. Malliakas for helpful discussions. This work was supported by the US Department of Energy, Office of Science, Basic Energy Sciences, Materials Science and Engineering Division. ChemMatCARS Sector 15 is principally supported by the Divisions of Chemistry (CHE) and Materials Research (DMR), National Science Foundation, under Grant NSF/CHE-1346572. Use of the Advanced Photon Source, an Office of Science User Facility operated for the US Department of Energy (DOE) Office of Science by Argonne National Laboratory, was supported by the US DOE under Contract DE-AC02-06CH11357.

1. Goodenough JB (2004) Electronic and ionic transport properties and other physical aspects of perovskites. *Rep Prog Phys* 67(11):1915–1993.
2. Imada M, Fujimori A, Tokura Y (1998) Metal-insulator transitions. *Rev Mod Phys* 70(4): 1039–1263.
3. Austin IG, Mott NF (1970) Metallic and nonmetallic behavior in transition metal oxides. *Science* 168(3927):71–77.
4. Goodenough JB (2014) Perspective on engineering transition-metal oxides. *Chem Mater* 26(1):820–829.
5. Coey M (2004) Condensed-matter physics: Charge-ordering in oxides. *Nature* 430(6996):155–157.
6. Ulbrich H, Braden M (2012) Neutron scattering studies on stripe phases in non-cuprate materials. *Physica C* 481(1):31–45.
7. Tranquada JM (2013) Spins, stripes, and superconductivity in hole-doped cuprates. *AIP Conf Proc* 1550(1):114–187.
8. Zaliznyak IA, Tranquada JM, Gu G, Erwin RW, Moritomo Y (2004) Universal features of charge and spin order in a half-doped layered perovskite. *J Appl Phys* 95(11):7369–7371.
9. Tranquada JM (1996) Stripe correlations of spins and holes in cuprates and nickelates. *Ferroelectrics* 177(1):43–57.
10. Boothroyd AT, Babkevich P, Prabhakaran D, Freeman PG (2011) An hour-glass magnetic spectrum in an insulating, hole-doped antiferromagnet. *Nature* 471(7338):341–344.
11. Cwik M, et al. (2009) Magnetic correlations in $La_{2-x}Sr_xCoO_4$ studied by neutron scattering: Possible evidence for stripe phases. *Phys Rev Lett* 102(5):057201.
12. Sakiyama N, Zaliznyak IA, Lee SH, Mitsui Y, Yoshizawa H (2008) Doping-dependent charge and spin superstructures in layered cobalt perovskites. *Phys Rev B* 78(18):180406.
13. Comin R, et al. (2015) Superconductivity. Broken translational and rotational symmetry via charge stripe order in underdoped $YBa_2Cu_3O_{6+y}$. *Science* 347(6228):1335–1339.
14. Abbamonte P, et al. (2005) Spatially modulated 'Mottness' in $La_{2-x}Ba_xCuO_4$. *Nat Phys* 1(3):155–158.
15. Vojta M, Vojta T, Kaul RK (2006) Spin excitations in fluctuating stripe phases of doped cuprate superconductors. *Phys Rev Lett* 97(9):097001.
16. Ikeda Y, et al. (2015) Transport and thermodynamic studies of stripe and checkerboard ordering in layered nickel oxides $R_{2-x}Sr_xNiO_4$ (R = La and Nd). *J Phys Soc Jpn* 84(2):023706.
17. Anissimova S, et al. (2014) Direct observation of dynamic charge stripes in $La_{2-x}Sr_xNiO_4$. *Nat Commun* 5:3467.
18. Hücker M, et al. (2006) Unidirectional diagonal order and three-dimensional stacking of charge stripes in orthorhombic $Pr_{1.67}Sr_{0.33}NiO_4$ and $Nd_{1.67}Sr_{0.33}NiO_4$. *Phys Rev B* 74(8):085112.
19. Lee SH, Cheong SW (1997) Melting of quasi-two-dimensional charge stripes in $La_{5/3}Sr_{1/3}NiO_4$. *Phys Rev Lett* 79(13):2514–2517.
20. Ulbrich H, et al. (2011) Evidence for charge orbital and spin stripe order in an overdoped manganite. *Phys Rev Lett* 106(15):157201.
21. Popović Z, Satpathy S (2002) Charge stacking in the half-doped manganites. *J Appl Phys* 91(10):8132–8134.
22. Sun Z, et al. (2011) Localization of electrons due to orbitally ordered bi-stripes in the bilayer manganite $La_{2-2x}Sr_{1+2x}Mn_2O_7$ ($x \sim 0.59$). *Proc Natl Acad Sci USA* 108(29): 11799–11803.
23. Abeykoon AMM, et al. (2013) Evidence for short-range-ordered charge stripes far above the charge-ordering transition in $La_{1.67}Sr_{0.33}NiO_4$. *Phys Rev Lett* 111(9):096404.
24. Woo H, et al. (2005) Mapping spin-wave dispersions in stripe-ordered $La_{2-x}Sr_xNiO_4$ (x=0.275, 0.333). *Phys Rev B* 72(6):064437.
25. Yoshizawa H, et al. (2000) Stripe order at low temperatures in $La_{2-x}Sr_xNiO_4$ with $0.289 \leq x \leq 0.5$. *Phys Rev B* 61(2):R854–R857.
26. Zachar O, Kivelson SA, Emery VJ (1998) Landau theory of stripe phases in cuprates and nickelates. *Phys Rev B* 57(3):1422–1426.
27. Cheong SW, et al. (1994) Charge-ordered states in $(La,Sr)_2NiO_4$ for hole concentrations n_h=1/3 and 1/2. *Phys Rev B* 49(10):7088–7091.
28. Chen CH, Cheong SW, Cooper AS (1993) Charge modulations in $La_{2-x}Sr_xNiO_{4+y}$: Ordering of polarons. *Phys Rev Lett* 71(15):2461–2464.
29. Anisimov VI, Bukhvalov D, Rice TM (1999) Electronic structure of possible nickelate analogs to the cuprates. *Phys Rev B* 59(12):7901–7906.
30. Poltavets VV, et al. (2006) $La_3Ni_2O_6$: A new double T′-type nickelate with infinite $Ni^{1+/2+}O_2$ layers. *J Am Chem Soc* 128(28):9050–9051.
31. ApRoberts-Warren N, et al. (2013) NMR evidence for spin fluctuations in the bilayer nickelate $La_3Ni_2O_6$. *Phys Rev B* 88(7):075124.
32. Lacorre P (1992) Passage from T-type to T′-type arrangement by reducing $R_4Ni_3O_{10}$ to $R_4Ni_3O_8$ (R = La, Pr, Nd). *J Solid State Chem* 97(2):495–500.
33. Retoux R, Rodriguez-Carvajal J, Lacorre P (1998) Neutron diffraction and TEM studies of the crystal structure and defects of $Nd_4Ni_3O_8$. *J Solid State Chem* 140(2):307–315.
34. Poltavets VV, et al. (2007) Crystal structures of $Ln_4Ni_3O_8$ (Ln = La, Nd) triple layer T′-type nickelates. *Inorg Chem* 46(25):10887–10891.
35. Poltavets VV, et al. (2010) Bulk magnetic order in a two-dimensional Ni^{1+}/Ni^{2+} (d^9/d^8) nickelate, isoelectronic with superconducting cuprates. *Phys Rev Lett* 104(20):206403.
36. ApRoberts-Warren N, et al. (2011) Critical spin dynamics in the antiferromagnet $La_4Ni_3O_8$ from ^{139}La nuclear magnetic resonance. *Phys Rev B* 83(1):014402.
37. Cheng JG, et al. (2012) Pressure effect on the structural transition and suppression of the high-spin state in the triple-layer T′-$La_4Ni_3O_8$. *Phys Rev Lett* 108(23):236403.
38. Pardo V, Pickett WE (2010) Quantum confinement induced molecular correlated insulating state in $La_4Ni_3O_8$. *Phys Rev Lett* 105(26):266402.
39. Sarkar S, Dasgupta I, Greenblatt M, Saha-Dasgupta T (2011) Electronic and magnetic structures of bilayer $La_3Ni_2O_6$ and trilayer $La_4Ni_3O_8$ nickelates from first principles. *Phys Rev B* 84(18):180411.
40. Liu T, et al. (2012) Electronic structure and magnetism of $La_4Ni_3O_8$ from first principles. *J Phys Condens Matter* 24(40):405502.
41. Pardo V, Pickett WE (2012) Pressure-induced metal-insulator and spin-state transition in low-valence layered nickelates. *Phys Rev B* 85(4):045111.
42. Hua W (2013) Charge–spin–orbital states in the tri-layered nickelate $La_4Ni_3O_8$: An *ab initio* study. *New J Phys* 15(2):023038.
43. Liu T, et al. (2014) Dimensionality-induced insulator-metal crossover in layered nickelates $La_{n+1}Ni_nO_{2n+2}$ (n = 2, 3, and ∞). *AIP Adv* 4(4):047132.
44. Lokshin K, Egami T (2011) *Structure and Electronic Properties of the $La_4Ni_3O_8$*. Available at meetings.aps.org/link/BAPS.2011.MAR.T23.11. Accessed July 11, 2016.
45. Lee KW, Pickett WE (2004) Infinite-layer $LaNiO_2$: Ni^+ is not Cu^{2+}. *Phys Rev B* 70(16): 165109.
46. Ling CD, Argyriou DN, Wu G, Neumeier JJ (2000) Neutron diffraction study of $La_3Ni_2O_7$: Structural relationships among n=1, 2, and 3 phases $La_{n+1}Ni_nO_{3n+1}$. *J Solid State Chem* 152(2):517–525.
47. Li J, Zhu Y, Tranquada JM, Yamada K, Buttrey DJ (2003) Transmission-electron-microscopy study of charge-stripe order in $La_{1.725}Sr_{0.275}NiO_4$. *Phys Rev B* 67(1):012404.
48. Hayward MA, Green MA, Rosseinsky MJ, Sloan J (1999) Sodium hydride as a powerful reducing agent for topotactic oxide deintercalation: Synthesis and characterization of the nickel(I) oxide $LaNiO_2$. *J Am Chem Soc* 121(38):8843–8854.
49. Klingeler R, Büchner B, Cheong SW, Hücker M (2005) Weak ferromagnetic spin and charge stripe order in $La_{5/3}Sr_{1/3}NiO_4$. *Phys Rev B* 72(10):104424.
50. Ramirez AP, Gammel PL, Cheong SW, Bishop DJ, Chandra P (1996) Charge modulation in $La_{1.67}Sr_{0.33}NiO_4$: A bulk thermodynamic study. *Phys Rev Lett* 76(3):447–450.
51. Fawcett E, Alberts HL, Galkin VY, Noakes DR, Yakhmi JV (1994) Spin-density-wave antiferromagnetism in chromium alloys. *Rev Mod Phys* 66(1):25–127.
52. Wochner P, Tranquada JM, Buttrey DJ, Sachan V (1998) Neutron-diffraction study of stripe order in $La_2NiO_{4+\delta}$ (δ=2/15). *Phys Rev B* 57(2):1066–1078.
53. Tranquada JM, Buttrey DJ, Sachan V (1996) Incommensurate stripe order in $La_{2-x}Sr_xNiO_4$ with x=0.225. *Phys Rev B* 54(17):12318–12323.
54. Kato M, Maeno Y, Fujita T (1991) Two-dimensional antiferromagnetic correlation with spin 1/2 in magnetic susceptibility of $(La, Sr)_2NiO_4$. *Physica C* 176(4):533–540.
55. Lubashevsky Y, Keren A (2008) Experimental investigation of the origin of the crossover temperature in cuprate superconductors via dc magnetic susceptibility. *Phys Rev B* 78(2):020505.
56. Larson AC, Von Dreele RB (2004) *General Structure Analysis System (GSAS)* (Los Alamos National Laboratory, Los Alamos, NM), Tech Rep LAUR 86-748.
57. Toby BH (2001) EXPGUI, a graphical user interface for GSAS. *J Appl Crystallogr* 34(2): 210–213.
58. Stephens PW (1999) Phenomenological model of anisotropic peak broadening in powder diffraction. *J Appl Crystallogr* 32(2):281–289.
59. Bruker AXS, Inc. (2014) *APEX2* (Bruker AXS, Inc., Madison, WI).
60. Bruker AXS, Inc. (2014) *SHELXTL* (Bruker AXS, Inc., Madison, WI).